GEOPHYSICAL RESEARCH LETTERS, VOL. 40, 3074–3079, doi:10.1002/grl.50584, 2013

Field measurements and scaling of ocean surface wave-breaking statistics

Peter Sutherland[1] and W. Kendall Melville[1]

Received 30 April 2013; revised 21 May 2013; accepted 22 May 2013; published 17 June 2013.

[1] Deep-water breaking waves provide a mechanism for mass, momentum, and energy transfer between the atmosphere and ocean. Microscale breaking is particularly important, but notoriously difficult to measure in the field. In this paper, measurements from a new technique, using a stereo pair of long-wave infrared cameras to reconstruct the sea surface shape and velocity field, are presented. Breakers are detected using an image texture-based algorithm and then tracked on the reconstructed surface. These waves range from large air-entraining breakers to microbreakers that are undetectable by traditional visible video-based techniques. This allows measurements of breaker length distributions, $\Lambda(c)$, that extend to velocities near the gravity-capillary transition. These distributions are compared with measurements from the literature and from visible video imagery. A nondimensional scaling is proposed which collapses $\Lambda(c)$. Finally, estimates of energy dissipation and stress based on $\Lambda(c)$ are found to agree well with wave energy dissipation and wind stress models. **Citation:** Sutherland, P., and W. K. Melville (2013), Field measurements and scaling of ocean surface wave-breaking statistics, *Geophys. Res. Lett.*, *40*, 3074–3079, doi:10.1002/grl.50584.

1. Introduction

[2] The air-sea interface has a profound effect on weather and climate, with deep-water breaking waves playing an important role [*Banner and Peregrine*, 1993; *Melville*, 1996; *Duncan*, 2001]. Energy dissipation by breakers limits growth of the surface wave field and provides a mechanism for momentum transfer from waves to currents. Bubbles and aerosols produced by breaking support gas and heat transfer between the ocean and atmosphere. Breaking statistics are very difficult to simulate in the laboratory or to model numerically and so field measurements are necessary for progress.

[3] *Phillips* [1985] defined a distribution of breaker front length $\Lambda(\boldsymbol{c})$ per unit area of sea surface per unit increment of breaking front velocity $\boldsymbol{c}(c, \theta)$, where c and θ are the speed and direction of breaker front propagation, respectively. The moments of $\Lambda(\boldsymbol{c})$ have important physical interpretations. The fraction of surface area turned over by breaking fronts per unit time is the first moment of $\Lambda(c)$ [*Phillips*, 1985]

$$R = \int c\Lambda(c)\mathrm{d}c, \tag{1}$$

which is related to heat and gas transfer between the ocean and the atmosphere [*Jessup et al.*, 1997].

[4] *Phillips* [1985] showed that the average rate of gravity wave energy loss per unit area by breakers with velocities between $\boldsymbol{c}$ and $\boldsymbol{c} + d\boldsymbol{c}$ can be written,

$$\epsilon(\boldsymbol{c})d\boldsymbol{c} = bg^{-1}\rho_w c^5 \Lambda(\boldsymbol{c})\mathrm{d}\boldsymbol{c}. \tag{2}$$

where g is the gravitational acceleration, ρ_w is the water density, $\boldsymbol{c}$ is the breaker front velocity, and b is the dimensionless breaking parameter.

[5] Integrating over all breaker speeds c, the fifth moment of $\Lambda(c)$ gives the total gravity wave energy dissipated by breaking waves per unit area of ocean surface,

$$F_E = \frac{\rho_w}{g}\int bc^5\Lambda(c)\mathrm{d}c. \tag{3}$$

Similarly, the fourth moment of $\Lambda(\boldsymbol{c})$ yields the momentum flux from the wave field into the upper ocean,

$$\boldsymbol{F_m} = \frac{\rho_w}{g}\int bc^3\boldsymbol{c}\Lambda(\boldsymbol{c})\mathrm{d}\boldsymbol{c}. \tag{4}$$

Phillips [1985] used a constant value for b and, by assuming an equilibrium wave spectrum, predicted that $\Lambda(c) \propto c^{-6}$. More recent laboratory work using focusing wave packets [*Melville*, 1994; *Banner and Peirson*, 2007; *Drazen et al.*, 2008] has shown that b varies over at least three orders of magnitude. For plunging breakers, *Drazen et al.* [2008] predicted that b is proportional to $S^{5/2}$, where S is the linear focusing slope at breaking. *Romero et al.* [2012] showed that $b = 0.4(S - 0.08)^{5/2}$ fits all available laboratory data, from incipient to plunging breaking, and used it to create a semi-empirical spectral model of the breaking parameter in the field,

$$b(k) = A_1(B(k)^{1/2} - B_T^{1/2})^{5/2}. \tag{5}$$

Here $B(k)$ is the azimuth-integrated saturation spectrum, with the wave number k related to c using the linear dispersion relation for deep-water gravity waves. B_T and A_1 are constants that were determined by balancing wave field dissipation [*Romero and Melville*, 2010] with the dissipation from breaking calculated with equation (2), using the field measurements of $\Lambda(c)$ by *Kleiss and Melville* [2010]. This model for $b(k)$ was used by *Romero et al.* [2012] to predict a form of $\Lambda(c)$, at low c values, that extended roughly from the peak of the field measurements of

Additional supporting information may be found in the online version of this article.

[1]Scripps Institution of Oceanography, University of California, San Diego, La Jolla, California, USA.

Corresponding author: P. Sutherland, Scripps Institution of Oceanography, University of California, San Diego, La Jolla, CA 92093-0213, USA. (sutherlandp@ucsd.edu)

0094-8276/13/10.1002/grl.50584

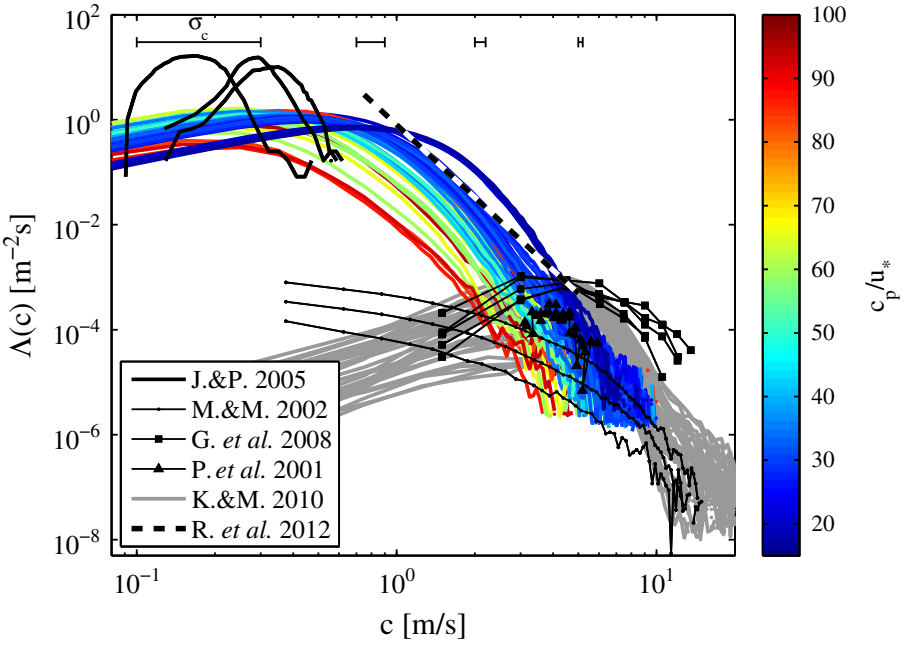

Figure 1. Measured $\Lambda(c)$ compared with the literature. Lines colored by wave age are from this work. Thick black lines are from the laboratory measurements of *Jessup and Phadnis* [2005]. Field measurements are from *Melville and Matusov* [2002] lines with small dots, *Gemmrich et al.* [2008] lines with squares, *Phillips et al.* [2001] lines with triangles, and *Kleiss and Melville* [2010] solid gray lines. The black and white dashed line is the modeled extrapolation by *Romero et al.* [2012] of the measurements of *Kleiss and Melville* [2010]. Horizontal bars near the top indicate standard deviation of velocity error calculated using synthetic data.

Kleiss and Melville [2010] to the peak of the laboratory measurements of *Jessup and Phadnis* [2005].

[6] Several studies have undertaken direct measurements of $\Lambda(\boldsymbol{c})$ in the field, as summarized in Figure 1. Although early work by *Phillips et al.* [2001] used radar backscatter, all field measurements since then have used video imagery of the sea surface. *Melville and Matusov* [2002] and *Kleiss and Melville* [2010, 2011] used airborne imagery, while *Gemmrich et al.* [2008] and *Thomson et al.* [2009] used platform-based measurements.

[7] Detection of breakers in video imagery relies on whitecaps being much brighter than the surrounding ocean due to the scattering of light by entrained bubbles and foam. Microscale breakers do not entrain air, and so are essentially undetectable by visible imagery. They do, however, mix the cool skin layer with warmer water below, so their warm actively breaking front and wake can be detected in IR imagery [*Zappa et al.*, 2001]. *Jessup and Phadnis* [2005] used IR video to image wind-generated microscale breakers in the laboratory. Their measured $\Lambda(c)$ showed a much higher density of breakers at lower speeds than previous visible video-based fieldwork.

[8] The primary goal of this work is to include microscale breakers in field measurements of $\Lambda(c)$. This has been achieved by using stereo IR measurements to capture breaking waves in the open sea. To the authors' knowledge, it represents the first successful inclusion of microscale breakers in field measurements of $\Lambda(\boldsymbol{c})$.

2. Experiment and Methods

[9] The data described here were collected during three deployments of Research Platform *FLIP* in the Pacific Ocean in 2009 and 2010. Radiance in a Dynamic Ocean 2009, RaDyO 2009, [*Dickey et al.*, 2012], was a 12-day deployment that started 120 km south of the Island of Hawai'i with *FLIP* drifting west at approximately 35 cm/s (0.7 knots) for approximately 330 km in typical trade winds. The Office of Naval Research-sponsored High Resolution Air-Sea Interaction Departmental Research Initiative consisted of two experiments: The main experiment, HiRes, 2010 was a 14 day deployment with *FLIP* moored approximately 25 km off the coast of Northern California (38°20′N, 123°26′W) in strong northwesterly winds. The second experiment, SoCal 2010, took place over 2 days in the Southern California Bight in much milder conditions. Between the three experiments, 70 20-minute records were analyzed with wind speeds, U_{10}, of 1.6 to 16 m/s, significant wave heights, H_s, of 0.7 to 4.7 m, and wave ages, c_p/u_*, of 16 to 150 (where c_p is the phase speed of waves at the spectral peak and u_* is the atmospheric friction velocity).

[10] The primary instrumentation was a pair of FLIR SC6000 long-wave infrared (8–9.2 μm) video cameras. The cameras were mounted 3 m apart on a horizontal spar at the end of one of *FLIP*'s booms. The cameras were angled slightly toward each other so that they shared the same field of view on the sea surface and angled 20° from vertical away from *FLIP* in order to reduce reflections from *FLIP*'s superstructure and booms. The colocated field of view was approximately 4 × 3 m, and the image size of 640 × 512 pixels resulted in a nominal resolution of approximately 6 mm (which changed depending on the instantaneous boom and surface displacement). IR video was captured at 40 Hz (sub-sampled at 20 Hz) for the first 20 min of every hour.

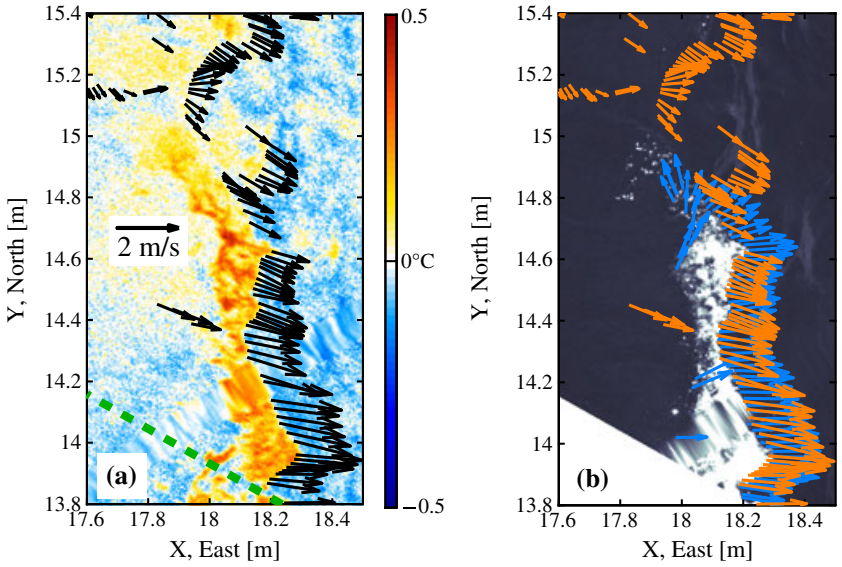

Figure 2. Snapshot of a breaker detected in co-located visible and IR imagery, taken during SoCal 2010 experiment, December 6, 2010, 22:02:32.75 [UTC]. (a) IR temperature image with 20-minute mean removed. Black arrows indicate breaking front velocities [m/s] (scale given in image), green dashed line indicates the boundary of the cutout in the visible image (white area in Figure 2b). (b) Visible (black and white) image. Blue arrows indicate breaking front velocities detected in visible imagery, orange arrows indicate velocities detected in IR. The white area in the lower left was removed from analysis as it contained a subsurface instrument which was visible through the clear ocean water and thus affected breaker detection in visible imagery. Wide field of view versions of these images are available in Supplementary Figures 4 and 5.

[11] Over the duration of these experiments, the sea surface contained a wide variety of thermal structures that were detectable by the IR cameras (i.e., temperature differences greater than the detectable minimum of approximately 25 mK). These structures included actively breaking waves, remnants of past breakers, and the surface signatures of convective and other turbulence. By matching these features in both stereo images, it was possible to triangulate the location of the features in 3-D. The use of IR imagery in the laboratory [*Hilsenstein*, 2005] has shown it to be an effective way of eliminating the principal difficulties of using visible stereo on a water surface, namely water penetration and specular reflection [*Jähne et al.*, 1994]. By assuming that these same temperature structures behaved as passive tracers over the time scale of the video frame separation (0.05 s), and tracking them between consecutive frames, it was possible to derive the water surface velocity. Further details of the stereo thermal structure particle imaging velocimetry (PIV) processing are available in the supporting information. This thermal structure PIV technique has been used by other authors [*Garbe et al.*, 2003; *Veron et al.*, 2008; *Rocholz et al.*, 2010] to measure surface velocity with a single IR camera (under the assumption of a flat sea surface), but to the best of our knowledge, has never before been combined with stereo IR imaging to reconstruct the 3-D velocity at the sea surface.

[12] In addition to stereo IR imagery, a variety of supporting measurements were taken. Colocated stereo visible video was recorded for part of the SoCal 2010 experiment. Winds and atmospheric fluxes were measured with a CSAT3 3-D sonic anemometer eddy flux system (Campbell Scientific) mounted directly over the IR cameras' fields of view.

2.1. Breaker Detection

[13] In this work, a new technique was developed for breaker detection. Temperature structure in the actively breaking region and turbulent wake of a breaker is less uniform than that in the background surface field. One measure of non-uniformity in an image is "entropy," which is frequently used in the computer vision and synthetic aperture radar communities to quantify image texture (e.g., *Gonzalez et al.* [2009], *Holmes et al.* [1984]). Local entropy was used to detect breaking waves in infrared imagery. The supporting information contains a description of the technique and the method used to calculate $\Lambda(c)$. Four 10 min periods of visible video data, corresponding to the first half of their associated IR sampling periods, were also analyzed for comparison. The technique used for visible imagery was based on that developed by *Kleiss and Melville* [2011] and is described in the supporting information. An example of a breaker detected in both visible and IR imagery can be seen in Figure 2 and Figures S4 and S5. Note that the main bubble-entraining "whitecap" is obvious in both visible and IR images, with both measurements finding the actively breaking front in the same location with very similar velocities. However, the IR image shows the main breaker extending in the y direction well beyond the visible whitecap boundary and also shows several other smaller breakers that are completely undetected in the visible image.

3. Results

[14] The $\Lambda(c)$ measurements taken here are shown in Figure 1. They show, at the higher speeds, a similar functional dependence on c when compared to other examples from the literature. What sets the measurements in this

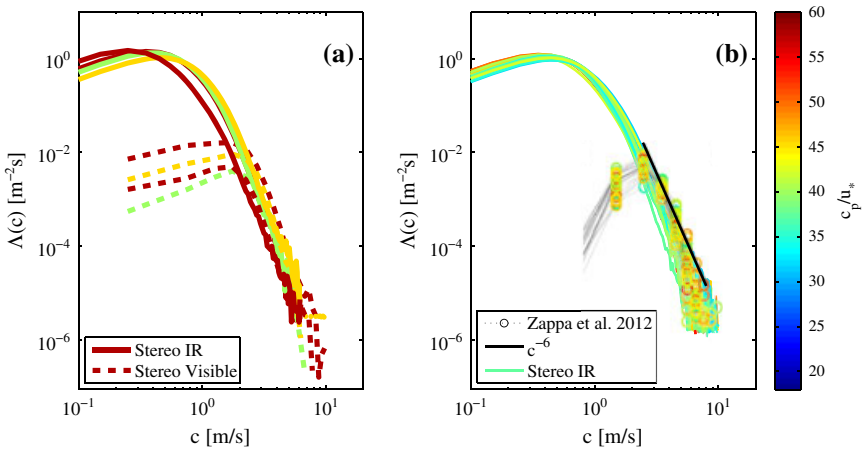

Figure 3. Comparison of $\Lambda(c)$ measured using visible and IR video. Color corresponds to wave age. (a) Distributions from concurrent, colocated IR video (solid lines) and visible video (dashed lines) taken during the SoCal 2010 experiment. (b) $\Lambda(c)$ measured during the RaDyO 2009 experiment using stereo IR (colored lines) compared with $\Lambda(c)$ measured during the same experiment by *Zappa et al.* [2012] using visible imagery (colored circles). The solid black line is the c^{-6} dependence predicted by *Phillips* [1985] as shown in *Zappa et al.* [2012].

work apart is their low-speed behavior, extending the field measurements of *Melville and Matusov* [2002], *Gemmrich et al.* [2008], *Kleiss and Melville* [2010], and others. They also appear to have a similar peak speed to the laboratory measurements of *Jessup and Phadnis* [2005] though that agreement may be coincidental.

[15] A recurring question in the literature is whether or not $\Lambda(c)$ should roll-off below some breaking speed c [*Gemmrich et al.*, 2008; *Kleiss and Melville*, 2011]. As can be seen in Figure 3, including microscale breakers has a very large effect on the level of $\Lambda(c)$ at low c. Both visible and IR measurements capture breaking fronts well for breakers with speeds above 2–3 m/s. Below that speed, visible measurements fail, likely due to the lack of air entrainment. The IR measurements presented here do not display a similar roll-off until c reaches between 10 and 80 cm/s. The standard deviation of velocity error was calculated to be approximately 20 cm/s (see supporting information), which likely broadens the peak in the $\Lambda(c)$ distributions. Further supporting the general form of these low c results is their similarity to the modeling work of *Romero et al.* [2012]. By using a theoretical extrapolated wave saturation spectrum, they predicted that $\Lambda(c)$ given by *Kleiss and Melville* [2010] should increase from the measured peak as c decreases, as shown in Figure 1.

4. Scaling $\Lambda(c)$

[16] A dimensional analysis of the dependence of $\Lambda(c)$ on the other variables and parameters leads to an improved understanding of the breaking process. $\Lambda(c)$ can be written as $\Lambda(c; \rho_a, \rho_w, u_*, g, c_p, H_s, \Gamma, X)$, where ρ_a is the air density, u_* is the atmospheric friction velocity, c_p is the phase speed of waves at the peak of the wind-wave spectrum, H_s is the significant wave height, Γ is the surface tension, and X is the wave fetch. Dimensional analysis then yields

$$\Lambda(c)c_p^3 g^{-1} = f\left(\frac{c}{\sqrt{gH_s}}, \frac{\rho_a}{\rho_w}, \frac{c_p}{u_*}, \frac{gH_s}{c_p^2}, \frac{gX}{c_p^2}, Bo\right), \quad (6)$$

Here $\sqrt{gH_s}$ is the speed attained in a ballistic trajectory from a height of $H_s/2$, c_p/u_* is the wave age, gH_s/c_p^2 is the wave steepness, gX/c_p^2 is the dimensionless fetch, and Bo is the Bond number. The spectral Bond number, $Bo = (\rho_w - \rho_a)c^4/g\Gamma$ is greater than 10 for $c > 29$ cm/s, implying that surface tension effects are negligible for speeds larger than this. Our RMS error in c is ± 20 cm/s, so surface tension effects are negligible over most of the range

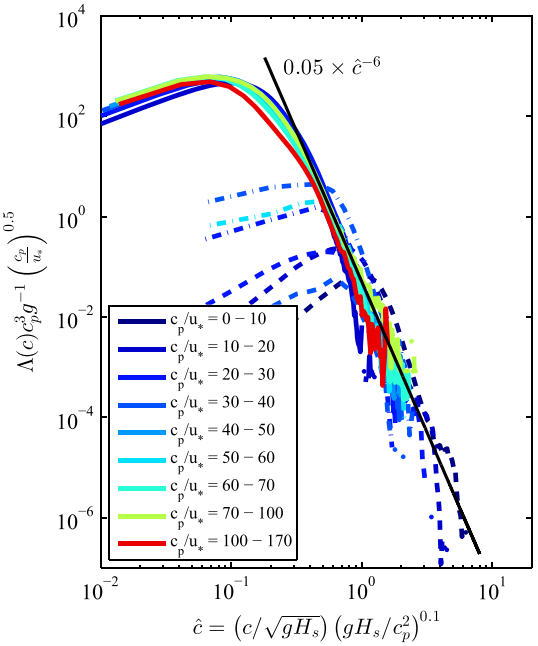

Figure 4. Nondimensional breaking length distribution. Distributions have been binned by wave age with corresponding colors. Solid lines (——) are measurements taken in this work using stereo IR imagery, dash-dotted (—·—) lines are from visible imagery in this work, and dashed lines (— —) are from the airborne measurements of *Kleiss and Melville* [2010]. Scaling uses ballistic velocity, steepness, and wave age dependence from equation (9).

of c and are neglected in this analysis. However, since the ratio $(\rho_w - \rho_a)/g\Gamma$ remained effectively constant over all experiments, these measurements had no significant Bond number dependence. Neglecting the Bond number, assuming that ρ_a/ρ_w is approximately constant, and assuming that in fetch-limited conditions X can be related to c_p, H_s, u_*, and g, equation (6) can be simplified to

$$\Lambda(c)c_p^3 g^{-1} = f\left(\frac{c}{\sqrt{gH_s}}; \frac{c_p}{u_*}, \frac{gH_s}{c_p^2}\right). \quad (7)$$

Assigning the wave age dependence to the ordinate and the steepness dependence to the abscissa, and assuming a power law dependence on both wave age and steepness, gives

$$\Lambda(c)\frac{c_p^3}{g}\left(\frac{c_p}{u_*}\right)^{\alpha} = f\left(\frac{c}{\sqrt{gH_s}}\left(\frac{gH_s}{c_p^2}\right)^{\gamma}\right). \quad (8)$$

Applying this scaling to all the stereo IR $\Lambda(c)$ distributions of Figure 1 and then varying α and γ to collapse the curves (by minimizing a squared-difference cost function) gave values of $\alpha = 0.5$ and $\gamma = 0.1$. Using those values, it is then possible to rewrite equation (8) as

$$\Lambda(c)\frac{c_p^3}{g}\left(\frac{c_p}{u_*}\right)^{0.5} = f\left(\frac{c}{\sqrt{gH_s}}\left(\frac{gH_s}{c_p^2}\right)^{0.1}\right) = f(\hat{c}), \quad (9)$$

where $\hat{c}$ is the scaled breaker front speed. This form of $\hat{c}$ suggests that the relevant velocity for scaling breaker front length distributions is $\sqrt{gH_s}$, with a weak dependence on the peak wave steepness, $H_s k_p = gH_s/c_p^2$. The ballistic velocity, $\sqrt{gH_s}$, has been used by previous authors for scaling breaking processes. *Drazen et al.* [2008] used it along with inertial scaling of dissipation to obtain the $S^{5/2}$ slope dependence of the breaking parameter that *Romero et al.* [2012] used to deduce equation (5).

[17] Figure 4 shows $\Lambda(c)$ measurements from stereo IR and stereo visible, as well as the airborne visible measurements of *Kleiss and Melville* [2010], scaled using equation (9). For speeds higher than the distribution peak, found between $\hat{c} = 0.06$ and 0.1, this scaling collapses all stereo IR measurements to a narrow curve. For larger speeds, that curve approaches $0.05 \times \hat{c}^{-6}$, exhibiting the power law dependence predicted by *Phillips* [1985]. One curve, corresponding to the range $c_p/u_* = 10 - 20$, fails to collapse as well as the others. Those data were taken during the HiRes 2010 experiment during which strong conditions and low air-water temperature differences reduced contrast in the IR imagery and made detection of breakers less reliable than in the other experiments. Thus, it is possible that the premature roll-off at low and high speeds of the $c_p/u_* = 10 - 20$ curve is due to measurement limitations rather than the breakers themselves.

[18] While the $\hat{c}^{-6}$ regions of the distributions measured using visible video show reasonable agreement with the high-speed region of the stereo IR distributions, the regions at velocities below the peaks of the visible video data, at approximately $\hat{c} = 0.8$, do not. This supports the hypothesis that the peaks found in $\Lambda(c)$ distributions measured using visible video are a result of their inability to measure breakers that do not entrain air. It also suggests that $\hat{c} = 0.8$ may be an important dynamic transition for air entrainment by breaking.

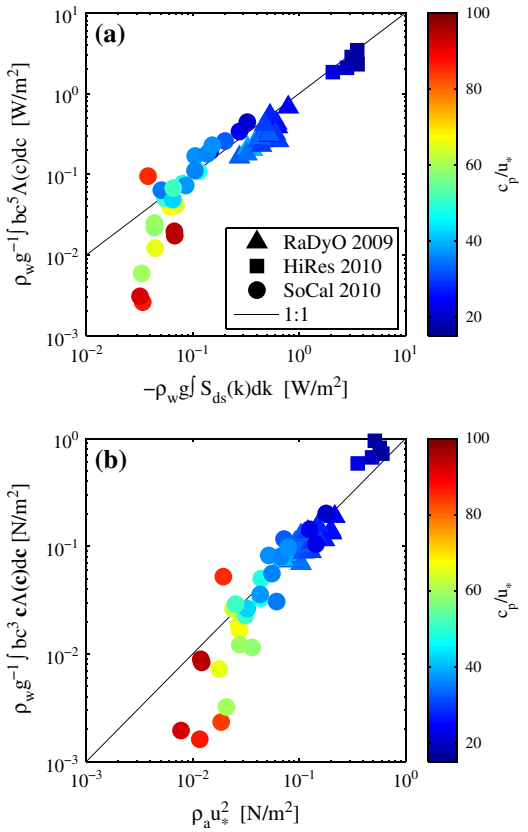

Figure 5. (a) Dissipation by breaking (ordinate) compared with modeled wave field dissipation (abscissa). (b) Momentum flux from waves to currents due to wave breaking (ordinate) plotted against wind stress (abscissa). Color shows wave age and solid line indicates 1:1 correspondence.

[19] The ability to nondimensionalize $\Lambda(c)$ over the wide range of wind and wave conditions in these experiments is an important step toward parameterization of wave-breaking statistics. Peak wave speed, friction velocity, and significant wave height are much more commonly and easily measured than $\Lambda(c)$.

5. Discussion

[20] Until this section, results have been presented with no assumptions made regarding the relationship between the speed of the breaking front c and the phase speed of the underlying wave c_w. However, *Phillips* [1985] and others have assumed that $c_w = ac$, where a is a constant of proportionality approximately equal to 1. In this discussion section, we explore the dynamics assuming $c_w = c$. Using equation (3), with the breaking parameter $b(k)$ as modeled in equation (5) and mapped to $b(c)$ using the linear dispersion relation for surface gravity waves, it is possible to estimate the total integrated dissipation by wave breaking. Since *Romero et al.* [2012] developed the expression for $b(c)$ in the context of surface gravity waves, $b(c)$ can only be used for speeds where the inclusion of surface tension has little effect. For the following analysis, the restriction of $c > 0.29$ m/s was applied, corresponding to wave num-

bers at which the spectral Bond number (section 4) is greater than 10.

[21] Figure 5a shows dissipation from measured breaking plotted against a model of the integrated spectral wave dissipation. The spectral wave dissipation model, S_{ds}, is from *Romero and Melville* [2010] and based on *Alves and Banner* [2003]. Wind input was calculated using the formulation of *Janssen* [1991]. Visually, agreement is good. For wave ages below $c_p/u_* = 50$, the relationship between dissipation by breaking and modeled dissipation is approximately linear. For very old waves, the linear relationship breaks down, suggesting that either breaking is not the dominant mechanism for wave dissipation, or the dissipation model fails, at high wave ages. Figure 5b shows that similarly momentum flux from breaking approaches equivalence with wind stress at low wave ages. The scatter in both the dissipation and stress is well within the scatter of the data used by *Romero et al.* [2012] to parameterize $b(k)$ in their model.

[22] **Acknowledgments.** These measurements would not have been possible without the exceptional engineering and field support of Luc Lenain and Nick Statom. We also thank Tom Golfinos, Bill Gaines, and the crew of *R/P FLIP* who always "went the extra mile." We thank Fabrice Veron and Zachary VanKirk for assisting with data collection during the HiRes 2010 experiment and for providing an early version of the stereo matching algorithm; Luc Lenain for providing useful video analysis software and much valuable advice; Laurent Grare for processing the meteorological data for the HiRes 2010 experiment; Jessica Kleiss for providing airborne $\Lambda(c)$ measurements from GOTEX, and Leonel Romero for many useful discussions and providing Matlab code for calculating model wind input. We are grateful for the efforts of the two anonymous reviewers whose insights greatly improved this paper. This research was conducted under grants to WKM from the Office of Naval Research (HiRes and RaDyO DRIs) and the National Science Foundation (Physical Oceanography).

[23] The Editor thanks two anonymous reviewers for their assistance in evaluating this paper.

References

Alves, J. H. G. M., and M. L. Banner (2003), Performance of a saturation-based dissipation-rate source term in modeling the fetch-limited evolution of wind waves, *J. Phys. Oceanogr.*, *33*, 1274–1298.

Banner, M., and W. L. Peirson (2007), Wave breaking onset and strength for two-dimensional deep-water wave groups, *J. Fluid Mech.*, *585*, 93–115.

Banner, M. L., and D. H. Peregrine (1993), Wave breaking in deep water, *Annu. Rev. Fluid Mech.*, *25*, 373–397.

Dickey, T., et al. (2012), Introduction to special section on recent advances in the study of optical variability in the near-surface and upper ocean, *J. Geophys. Res.*, *117*, C00H20, doi:10.1029/2012JC007964.

Drazen, D. A., W. K. Melville, and L. Lenain (2008), Inertial scaling of dissipation in unsteady breaking waves, *J. Fluid Mech.*, *611*, 307–332.

Duncan, J. H. (2001), Spilling breakers, *Annu. Rev. Fluid Mech.*, *33*, 519–547.

Garbe, C. S., H. Spies, and B. Jähne (2003), Estimation of complex motion from thermographic image sequences, in *Thermosense XXV, Proc. SPIE, Int. Soc. Opt. Eng.,* vol. 5073, pp. 303–317, edited by K. E. Cramer, and X. P. Maldague.

Gemmrich, J. R., M. L. Banner, and C. Garrett (2008), Spectrally resolved energy dissipation rate and momentum flux of breaking, *J. Phys. Oceanogr.*, *38*, 1296–1312.

Gonzalez, R. C., R. E. Woods, and S. L. Eddins (2009), *Digital Image Processing Using MATLAB*, Gatesmark, Knoxville, Tenn.

Hilsenstein, V. (2005), Surface reconstruction of water waves using thermographic stereo imaging, in *Proceedings of Image and Vision Computing New Zealand (IVCNZ 2005)*, pp. 102–107, Dunedin University of Otago , New Zealand, 28-29 Nov. 2005.

Holmes, Q. A., D. R. Nuesch, and R. A. Shuchman (1984), Textural analysis and real-time classification of sea-ice types using digital SAR data, *IEEE Trans. Geosci. Remote Sens.*, *GE-22*(2), 113–120.

Jähne, B., J. Klinke, and S. Waas (1994), Imaging of short ocean wind waves: A critical theoretical review, *J. Opt. Soc. Am. A*, *11*(8), 2197–2209.

Janssen, P. A. E. M. (1991), Quasi-linear theory of wind-wave generation applied to wave forecasting, *J. Phys. Oceanogr.*, *21*, 1631–1642.

Jessup, A. T., and K. R. Phadnis (2005), Measurement of the geometric and kinematic properties of microscale breaking waves from infrared imagery using a PIV algorithm, *Meas. Sci. Technol.*, *16*, 1961–1969.

Jessup, A. T., C. J. Zappa, M. R. Loewen, and V. Hesany (1997), Infrared remote sensing of breaking waves, *Nature*, *385*, 52–55.

Kleiss, J. M., and W. K. Melville (2010), Observations of wave breaking kinematics in fetch-limited seas, *J. Phys. Oceanogr.*, *40*, 2575–2604.

Kleiss, J. M., and W. K. Melville (2011), The analysis of sea surface imagery for white cap kinematics, *J. Atmos. Oceanic Technol.*, *28*, 219–243.

Melville, W. K. (1994), Energy dissipation in breaking waves, *J. Phys. Oceanogr.*, *42*(10), 2041–2049.

Melville, W. K. (1996), The role of surface-wave breaking in air-sea interaction, *Annu. Rev. Fluid Mech.*, *28*, 279–321.

Melville, W. K., and P. Matusov (2002), Distribution of breaking waves at the ocean surface, *Nature*, *417*, 58–63.

Phillips, O. M. (1985), Spectral and statistical properties of the equilibrium range in wind-generated gravity waves, *J. Fluid Mech.*, *156*, 505–531.

Phillips, O. M., F. L. Posner, and J. P. Hansen (2001), High range resolution radar measurements of the speed distribution of breaking events in wind-generated ocean waves: Surface impulse and wave energy dissipation rates, *J. Phys. Oceanogr.*, *31*, 450–460.

Rocholz, R., S. Wanner, U. Schimpf, and B. Jähne (2010), Combined visualization of wind waves and water surface temperature, in *The 6th International Symposium on Gas Transfer at Water Surfaces*, edited by S. Komori, W. McGillis, and R. Kurose, Kyoto University Press, Kyoto, Japan, 496–506.

Romero, L., and W. K. Melville (2010), Numerical modeling of fetch-limited waves in the Gulf of Tehuantepec, *J. Phys. Oceanogr.*, *3*, 466–486.

Romero, L., W. K. Melville, and J. M. Kleiss (2012), Spectral energy dissipation due to surface-wave breaking, *J. Phys. Oceanogr.*, *42*, 1421–1444.

Thomson, J., J. R. Gemmrich, and A. T. Jessup (2009), Energy dissipation and the spectral distribution of whitecaps, *Geophys. Res. Lett.*, *36*, L11601, doi:10.1029/2009GL038201.

Veron, F., W. K. Melville, and L. Lenain (2008), Infrared techniques for measuring ocean surface processes, *J. Atmos. Oceanic Technol.*, *25*, 307–326.

Zappa, C. J., W. E. Asher, and A. T. Jessup (2001), Microscale wave breaking and air-water gas transfer, *J. Geophys. Res.*, *106*(C5), 9385–9391, doi:10.1029/2000JC000262.

Zappa, C. J., M. L. Banner, H. Schultz, J. R. Gemmrich, R. P. Morison, D. A. LeBel, and T. Dickey (2012), An overview of sea state conditions and air-sea fluxes during RaDyO, *J. Geophys. Res.*, *117*, C00H19, doi:10.1029/2011JC007336.